IV
Displacements in Capillary Tubes

IV.1 Introduction

In this chapter the displacement by gas of a viscoplastic material, initially occupying the interior of a tube, is considered. This situation is encountered in applications such as the flow through porous media during enhanced oil recovery, coating flows, and the displacement of biological materials and pastes in different physiological systems (e.g. [64, 65, 66, 67]). Comprehensive reviews on capillary displacements are available in the literature [68, 69]. In these processes, it is important to understand the mechanism of material displacement and to determine the amount of material that is left behind adjacent to the wall. The configuration of the interface between the two materials depends on the relative role of viscous, elastic, and capillary forces near the interface.

Fairbrother and Stubbs [70] and Taylor [71] pioneered this subject by studying experimentally the Newtonian inertialess case. Their goal was to determine the fraction of mass deposited on the tube wall, m. Mass conservation allows m to be written in terms of the velocity of the tip of the interface, U, and the mean velocity, $\bar{u}$, of the liquid ahead (downstream) of the gas-liquid interface, *viz.*,

$$m = \frac{U - \bar{u}}{U} = 1 - \left(\frac{R_b}{R}\right)^2 \tag{1}$$

where R is the capillary tube radius and R_b is the bubble radius (Fig. IV.1). Taylor [71] studied the dependence of the mass fraction on the *capillary number*, $Ca \equiv \mu U/\sigma$, where μ and σ are the liquid Newtonian viscosity and surface tension, respectively. His analysis indicated that the amount of liquid deposited on the wall rises with the interface speed, and that m tends asymptotically to a value of 0.56 as Ca approaches 2. Cox [72] expanded the range of the capillary number up to 10, and showed that the asymptotic value

(as $Ca \rightarrow \infty$) is actually 0.60 for Newtonian liquids. Using the lubrication approximation, Bretherton [73] derived a theoretical correlation between the mass fraction and the capillary number, and the agreement between his predictions and Cox's experiments is good in the range of $10^{-3} < Ca < 10^{-2}$.

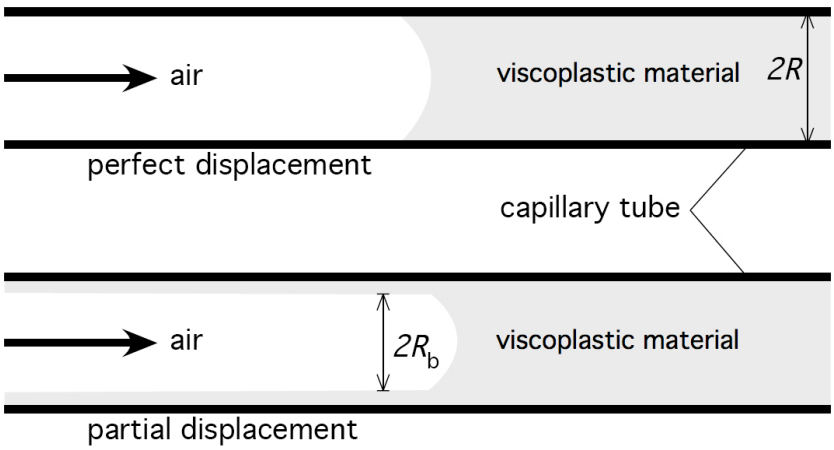

Figure IV.1: Displacement of a viscoplastic material in a capillary.

Giavedoni and Saita [74] reviewed the literature concerned with the theoretical modeling of gas-liquid displacement in the small gap between two parallel plates. They also presented a theoretical analysis of the steady displacement of a viscous liquid by a semi-infinite gas bubble using the finite element method, for capillary number values within the range 5×10^{-5} to 10. Lee et al. [75] used a finite-element method to study the steady gas displacement of viscoelastic materials confined between two parallel plates, while Quintella et al. [76] performed a similar study for the flow through capillaries.

The displacement of a material by another one has been first studied by Goldsmith and Mason [77], who reported experimental results on the amount of displaced material left on the tube wall as a function of different parameters, and showed that the mass fraction rises as the viscosity ratio is decreased. This trend agrees with their theoretical predictions and experimental data. Teletzke et al. [78] extended the work of Bretherton [73] to account for a viscous displacing fluid, and the effects of intermolecular forces in submicroscopically thin films. Their predictions, limited to $Ca < 10^{-4}$, agreed with the observation of Goldsmith and Mason [77], who showed that the film thickness of the displaced material left on the wall rises with the viscosity of the displacing fluid. Allouche et al. [79] reported a comprehensive study of the displacement of one yield-stress material by another in a plane channel. In this paper, the

authors discuss the conditions for the existence of static residual layers of the displaced material. Gabard [80] and Gabard and Hulin [81] report experiments and finite-volume calculations to determine the influence of rheology on the layer thickness of Carbopol dispersions displaced by water-glycerol solution in a 24-mm vertical tube (miscible displacement). They observed that the layer thickness decreases as the yield stress of the displaced material is increased. More recently, Soares et al. [82] analyzed, using finite-element simulations and experiments, the steady displacement of a viscous liquid by a long drop of another viscous liquid in a capillary tube, for a wide range of the capillary number and viscosity ratio. Their theoretical predictions and flow visualization experiments showed the effect of different parameters on the interface configuration and on the thickness of the layer of the displaced liquid left on the walls.

Regarding the gas displacement of viscoplastic materials, most of the articles available in the literature are concerned with Hele-Shaw cells, and in particular with the Saffman-Taylor instability. Alexandrou and Entov [83] analyzed the advancement and shape of bubbles in a Hele-Shaw cell previously occupied by Bingham materials. In a more recent study [84], this analysis is employed to the specific problem of the rising of a bubble in a cell filled with a Bingham material. Lindner et al. [85] showed that a modified capillary number containing the yield stress governs the Saffman-Taylor instability and determines the finger width. Finite-element simulations of the transient gas-displacement of Bingham (Papanastasiou) materials in straight and constricted tubes are reported by Dimakopoulos and Tsamopoulos [86]. For the high-capillary-number, inertialess displacement in tubes, they conclude that the deposited mass is quite insensitive to the Bingham number in the range investigated. The largest value of the Papanastasiou regularizing parameter employed to obtain their solutions corresponds to a jump number value of 150, as discussed later in this text.

This chapter reports experimental results for the displacement by air of a viscoplastic material in a capillary tube, as depicted in Fig. IV.1. The materials employed in the experiments were aqueous Carbopol dispersions. Their viscosity functions were well represented by a recently proposed four-parameter viscosity function [24]. In contrast to what happens for Newtonian and viscoelastic materials, it was observed that, for flow rates (or wall shear stresses) below a certain threshold value, the displacement is apparently perfect, i.e. no observable mass of material is left attached to the wall (Fig. IV.1). To help interpreting the experimental findings, the laminar fully-developed flow of viscoplastic materials in tubes was revisited to include

the interesting transition that occurs when the wall shear stress value is in the vicinity of the yield stress. This transition is closely related to the existence of the threshold wall shear stress values observed in the displacement experiments.

IV.2 Analysis

(a) Viscosity function and rheological parameters

The Carbopol dispersions present shear stress functions $\tau(\dot{\gamma})$ that are well represented by the following equation [24]:

$$\tau = \left(1 - \exp\left[-\frac{\eta_o \dot{\gamma}}{\tau_o}\right]\right)(\tau_o + K\dot{\gamma}^n) \tag{2}$$

in this equation, $\dot{\gamma}$ is the shear rate, while η_o, τ_o, K, and n, are respectively the low shear rate viscosity, the yield stress, the consistency index, and the behavior or power-law index. The physical meaning of these material parameters is discussed in detail by de Souza Mendes and Dutra [24].

According to Eq. (2), when the stress τ reaches the yield stress τ_o, there is a sharp increase of the shear rate with no appreciable change in stress, i.e. the shear stress remains roughly equal to τ_o while the shear rate value jumps from a value around $\dot{\gamma}_o$ to an often much larger value in the vicinity of $\dot{\gamma}_1$, where

$$\dot{\gamma}_o \equiv \frac{\tau_o}{\eta_o}; \quad \dot{\gamma}_1 \equiv \left(\frac{\tau_o}{K}\right)^{1/n} \tag{3}$$

De Souza Mendes [25] defined the jump number J, that gives a relative measure of the shear rate jump that occurs at $\tau = \tau_o$:

$$J \equiv \frac{\dot{\gamma}_1 - \dot{\gamma}_o}{\dot{\gamma}_o} = \frac{\eta_o \tau_o^{\frac{1-n}{n}}}{K^{1/n}} - 1 = \frac{\dot{\gamma}_1}{\dot{\gamma}_o} - 1 = \frac{1 - \dot{\gamma}_o^*}{\dot{\gamma}_o^*} \tag{4}$$

The jump number is a novel dimensionless rheological property of a given viscoplastic material. It combines the four rheological parameters (namely, τ_o, η_o, K, and n). The number of rheological properties that govern any flow of a viscoplastic material is thus reduced to two, n and J itself, both dimensionless. When $n = 1$, J becomes independent of the yield stress τ_o and reduces to

$J = \eta_o/K - 1$, i.e. for $n = 1$, $J + 1$ becomes the ratio between η_o and the plastic viscosity.

Choosing $\dot{\gamma}_1$ as characteristic shear rate and τ_o as the characteristic stress, so that $\tau^* \equiv \tau/\tau_o$ and $\dot{\gamma}^* \equiv \dot{\gamma}/\dot{\gamma}_1$ are respectively the dimensionless versions of the shear stress and shear rate, then the following dimensionless form of Eq. (2) can be written:

$$\tau^* = (1 - \exp[-(J+1)\dot{\gamma}^*])\,(1 + \dot{\gamma}^{*n}) \tag{5}$$

The dimensionless viscosity function is defined as

$$\eta^* = \frac{\tau^*}{\dot{\gamma}^*} = \frac{\eta}{\eta_o}(J+1) = (1 - \exp[-(J+1)\dot{\gamma}^*])\left(\frac{1}{\dot{\gamma}^*} + \dot{\gamma}^{*n-1}\right) \tag{6}$$

(b) Governing equations and boundary conditions

The parameters relevant to this physical situation are defined with the aid of its governing equations, which are written in dimensionless form. To this end, the following dimensionless variables are defined:

$$\boldsymbol{v}^* = \frac{\boldsymbol{v}}{\dot{\gamma}_1 R}; \quad \boldsymbol{T}^* = \frac{\boldsymbol{T}}{\tau_o}; \quad p^* = \frac{p}{\tau_o}; \quad \nabla^* = R\nabla \tag{7}$$

where R is the tube radius, $\boldsymbol{v}$ is the velocity field, $\boldsymbol{T}$ is the stress field, and p is the pressure field.

This flow is isochoric and attains a steady state when described from a reference frame attached to the bubble front. For this steady-state situation, the dimensionless mass and momentum conservation equations are:

$$\nabla^* \cdot \boldsymbol{v}^* = 0; \qquad \nabla^* \cdot \boldsymbol{T}^* = \boldsymbol{0} \tag{8}$$

In this analysis it is assumed that the material behaves like the generalized Newtonian material model [6], given by:

$$\boldsymbol{T}^* = -p^*\boldsymbol{1} + \eta^*(\dot{\gamma}^*)\dot{\boldsymbol{\gamma}}^* \tag{9}$$

where $\dot{\boldsymbol{\gamma}}^* = \nabla^*\boldsymbol{v}^* + (\nabla^*\boldsymbol{v}^*)^T$ is the rate-of-deformation tensor field, $\dot{\gamma}^* \equiv$

$\sqrt{tr\ \dot{\boldsymbol{\gamma}}^{*2}/2}$ is a measure of its intensity, and $\eta^*(\dot{\gamma}^*)$ is given by Eq. (6).

The boundary conditions are now described with the aid of Fig. IV.2. The no-slip/impermeability boundary condition is assumed at the tube wall, $\boldsymbol{v}^* = -U^*\hat{\boldsymbol{e}}_z$, where U^* is the (dimensionless) speed of the bubble front and $\hat{\boldsymbol{e}}_z$ is a unit vector in the axial direction. Each value of U^* implies a given value of $\tau_R^* \equiv \tau_R/\tau_o$, the wall shear stress far ahead of the bubble front, and hence either one (τ_R^* or U^*) can be chosen as the parameter related to the flow rate.

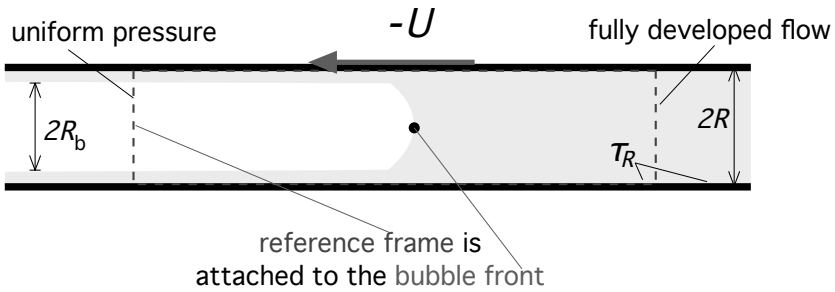

Figure IV.2: The boundary conditions as described from a reference frame attached to the bubble front.

Far upstream of the bubble front, the pressure is assumed to be uniform within the material layer and equal to p_{in}, i. e. $\boldsymbol{e}_z \cdot \boldsymbol{T}^* \cdot \boldsymbol{e}_z = -p_{in}/\tau_o$, where p_{in} is also dictated by U^* (or τ_R^*).

Far away downstream of the bubble front, fully developed flow is expected, i. e. $\boldsymbol{e}_z \cdot \boldsymbol{T}^* = \boldsymbol{0}$ on the downstream cross section.

At the interface, two boundary conditions are imposed. The first is a kinematic condition, $\boldsymbol{n} \cdot \boldsymbol{u}^* = 0$, where $\boldsymbol{n}$ is the local unit vector normal to the interface and pointing into the gas phase. The second condition arises from a stress balance, $\boldsymbol{n} \cdot \boldsymbol{T}^* = \boldsymbol{n}/(R_m^* Ca_p)$, where $R_m^* = R_m/R$ is the local mean curvature radius, and $Ca_p \equiv \tau_o R/\sigma$ is a parameter that gives the relative importance of yield stress and surface tension as far as the interface shape is concerned. This parameter is called the plastic capillary number.

(c) Governing parameters

The foregoing analysis indicates that this flow is governed by four dimensionless parameters. Two of these parameters are just rheological material properties, namely, the jump number, J, and the power-law exponent, n. The third parameter is the plastic capillary number, Ca_p, which depends on the yield stress, the surface tension, and the tube geometry.

The last parameter is a flow parameter, and there are a number of equivalent choices for it. One possible choice is the dimensionless wall shear stress far ahead of the bubble front, τ_R^*. Because the yield stress was taken as the characteristic stress, this parameter can also be seen as the reciprocal of a Bingham number. Another possible choice is the dimensionless average velocity of the material far ahead of the bubble front, $\bar{u}^*$. It is clear that there is a one-to-one relationship between $\bar{u}^*$ and τ_R^* (see Sec. IV.4(a) below). The dimensionless velocity of the bubble front, $U^* = \bar{u}^*/(1-m)$ is still another choice.

IV.3 The Experiments

(a) The displacement experiments

The displacement experiments are now described with the aid of Fig. IV.3. The main components of the test rig are an air tank, a Carbopol storage tank, a glass tube, and a glass box. The tube diameter is $2R = 3\,\text{mm}$, while its length is $L = 600\,\text{mm}$. During the visualization tests, the glass box that surrounds the tube is kept full with glycerin, to help eliminating image distortion due to refraction.

After the storage tank is loaded with a previously prepared and characterized Carbopol dispersion, both tanks are pressurized with the aid of the laboratory compressed air line. Pressostatic valves (not shown in Fig. IV.3) keep their pressure at a preselected constant value.

The flow-control valves are first set to allow the Carbopol dispersion to flow into the hose and then into the glass tube. When the latter is completely filled with the dispersion, the flow is interrupted, the tube (full with dispersion) is disconnected from the test section and then weighed in a 0.01 g-resolution balance. It is then reassembled into the flow circuit.

A new setting of the valves allows the air from the air tank to push the dispersion through the glass tube and out of the flow circuit. For different flow rates, the shape of the air-dispersion interface front is photographed with a CCD camera, and the total displacement time is recorded. An essentially constant speed U is obtained during the experiments by maintaining the valve downstream partially closed, thus ensuring that the dominant pressure drop in the flow circuit occurs past this valve.

After the bubble front has left the glass tube, the flow is stopped. The glass tube is disconnected from the flow circuit and then it is weighted again. The results of these two weighings (together with the weight of the clean tube)

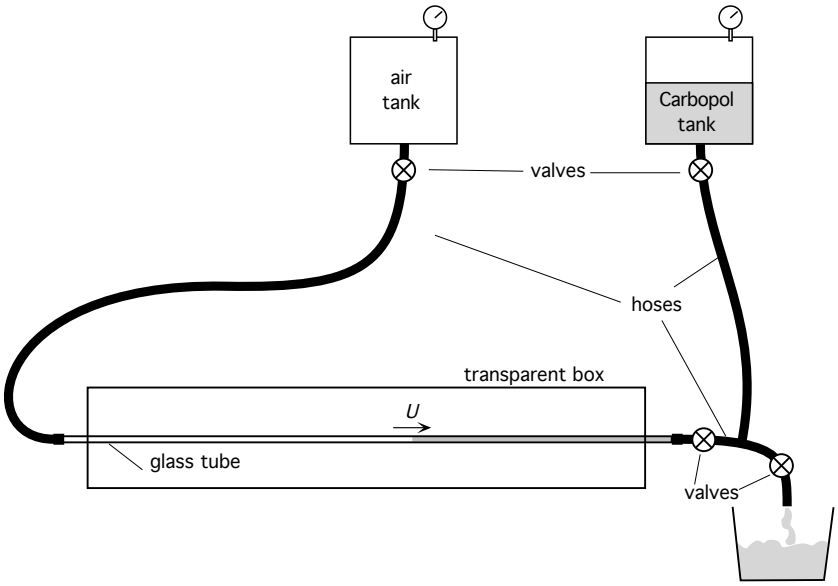

Figure IV.3: The experimental setup.

allow the determination of the fractional mass coverage m of the tube inner surface by taking the ratio of mass of dispersion remaining on the tube wall to the total mass of dispersion for the full tube:

$$m = \frac{\text{mass remaining}}{\text{total mass}} \tag{10}$$

The mass and time measurements allow the determination of the mass flow rate and the average velocity of the dispersion. The bubble front velocity U is also calculated with these data and with the aid of the continuity principle. The mass density of the Carbopol dispersions was measured with a calibrated picnometer, and the value obtained was $\rho = 999.6 \pm 0.2\,\mathrm{kg/m^3}$ for all dispersions.

The plastic capillary number $Ca_p = \tau_o R/\sigma$ was also evaluated for each Carbopol dispersion. The surface tension σ was measured with the aid of a platinum-ring tensiometer. This measurement was feasible for low-concentration dispersions only, and $\sigma = 0.06 \pm 0.005\,\mathrm{Pa.m}$ was obtained independently of the concentration. It was not possible to perform reliable measurements for high-concentration dispersions, and the value $\sigma = 0.06\,\mathrm{Pa.m}$ was assumed for all dispersions. This approximation seems to be of little importance in the evaluation of Ca_p because τ_o is expected to be a much stronger function of concentration than σ.

The shear stress at the wall, τ_R, appearing in the flow parameter $\tau_R^* = \tau_R/\tau_o$ was evaluated by obtaining, for each flow rate, the numerical solution of the momentum equation for the fully developed flow ahead of the bubble

front (see sec. IV.4(a) below). In the experiments, τ_R^* was varied by varying the air pressure and hence the flow rate. An uncertainty analysis yielded error estimates below 10% both for m and τ_R^*.

(b) Rheology of the Carbopol dispersions

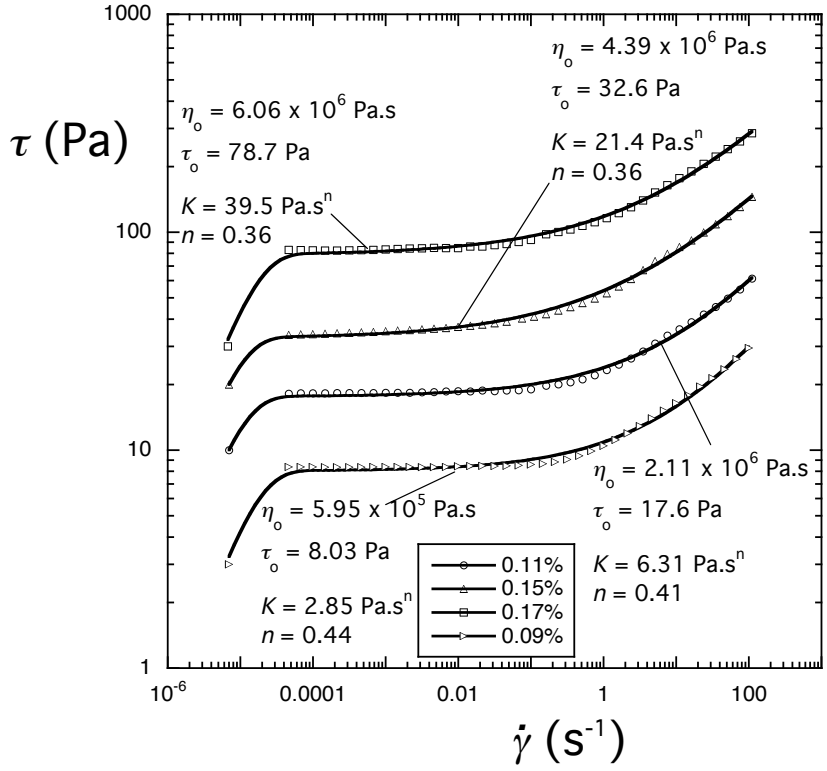

Figure IV.4: The flow curves of the Carbopol dispersions.

Aqueous dispersions of Carbopol 676 at different concentrations were employed in the flow experiments. The dispersions were NaOH-neutralized to achieve a pH of about 7. Right after preparation, the dispersions presented too many air bubbles, but after a few days at rest the small bubbles seem to dissolve into the dispersion. The viscosity function of these materials was obtained with an ARES rotational rheometer at controlled strain mode and a modified Couette geometry designed to circumvent possible apparent-slip problems (e.g. [21, 22]). The modification consists of the introduction of longitudinal grooves on both the bob and the cup surfaces. The grooves are 1-mm deep, 2-mm wide, and roughly 2-mm spaced. This geometry was successfully tested with standard Newtonian mineral oils. The results obtained essentially coincided with the corresponding ones obtained with smooth surfaces. Each data point was taken only after the steady state was achieved. The data-points corresponding to the lowest shear rate were obtained from creep experiments

performed in a UDS 200 Paar-Phisica rheometer, because the rate-sweep tests of the ARES rheometer employed could not handle such low shear rates. In these creep tests, a constant stress below the yield stress is imposed, and, after a steady flow is attained, typically after up to 48 hours, the corresponding shear rate is obtained. Flow curves were obtained both with fresh samples and with samples collected after the experiments, and no significant degradation signs were observed.

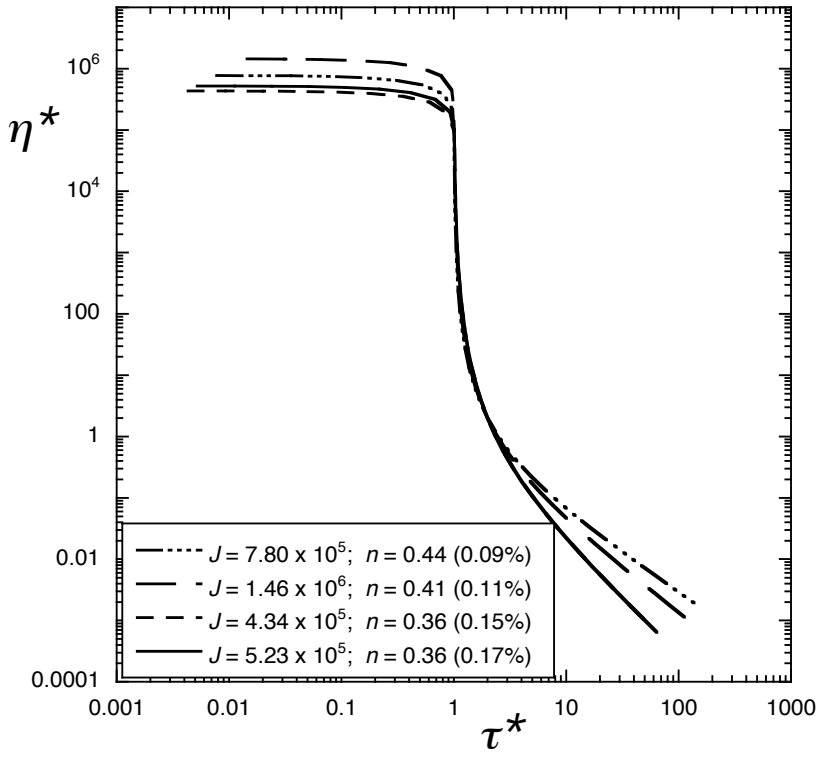

Figure IV.5: The dimensionless viscosity functions of the Carbopol dispersions.

The results obtained are shown in Fig. IV.4, together with the rheological parameters determined with curve fittings employing Eq. (2). These fittings are shown to reproduce well the data obtained. All materials present a clearly viscoplastic behavior, characterized by the shear rate jump at the yield stress.

Fig. IV.5 presents the viscosity functions of the Carbopol dispersions in dimensionless form, with their respective dimensionless rheological parameters. This figure shows that, in the range covered by the Carbopol dispersions investigated, the effect of power-law exponent n on the viscosity function is restricted to $\tau^* \gtrsim 8$. Therefore, when $\tau^* \lesssim 8$, the only relevant rheological parameter is the jump number J.

IV.4 Results and Discussion

(a) Results for the fully-developed flow

Before presenting the displacement results, it is important to examine the fully developed flow that occurs far downstream of the bubble front. This analysis was done by de Souza Mendes et al. [26].

For the fully developed flow through a tube of radius R, driven by an axial pressure gradient dp/dz, an overall force balance yields

$$-\tau_{r\theta}(R) = \tau(R) = \tau_R = -\frac{dp}{dz}\frac{R}{2} \tag{11}$$

The momentum conservation principle also dictates that the shear stress $\tau_{r\theta}$ is a linear function of the radial coordinate r. Thus, it is possible to write, in dimensionless form:

$$\tau^* = \tau_R^* r^* \tag{12}$$

For fully developed flow, the dimensionless shear rate is

$$\dot{\gamma}^* = -\frac{du^*}{dr^*} \tag{13}$$

where $u^* \equiv u/\dot{\gamma}_1 R$ is the dimensionless axial velocity. Combining Eqs. (5) and (12)

$$\tau_R^* r^* = \left(1 - \exp\left[-(J+1)\dot{\gamma}^*\right]\right)\left(1 + \dot{\gamma}^{*n}\right) \tag{14}$$

Equation (14) yields $\dot{\gamma}^*(r^*)$, which can be combined with Eq. (13) and integrated for the velocity profile $u^*(r^*)$. The integration is performed numerically with the aid of a non-uniform mesh of 2000 nodal points along the radial coordinate r^*. Half of the nodal points (1000) are concentrated in the region of high velocity gradients, namely, around the radial position $r_o^* = 1/\tau_R^*$ where $\tau^* = 1$. This mesh was shown to yield mesh-independent results for all cases investigated. To handle the non-linear nature of this equation, for each set of values of the parameters $\{\tau_R^*, J, n\}$, the following solution strategy is adopted:

1. for each nodal point, Eq. (14) is solved iteratively for $\dot{\gamma}^*$;

2. then Eq. (13) is integrated using the trapezoidal rule. The axial symmetry and no-slip boundary conditions, namely, $\dot{\gamma}^*(0) = 0$ and $u^*(1) = 0$ are employed.

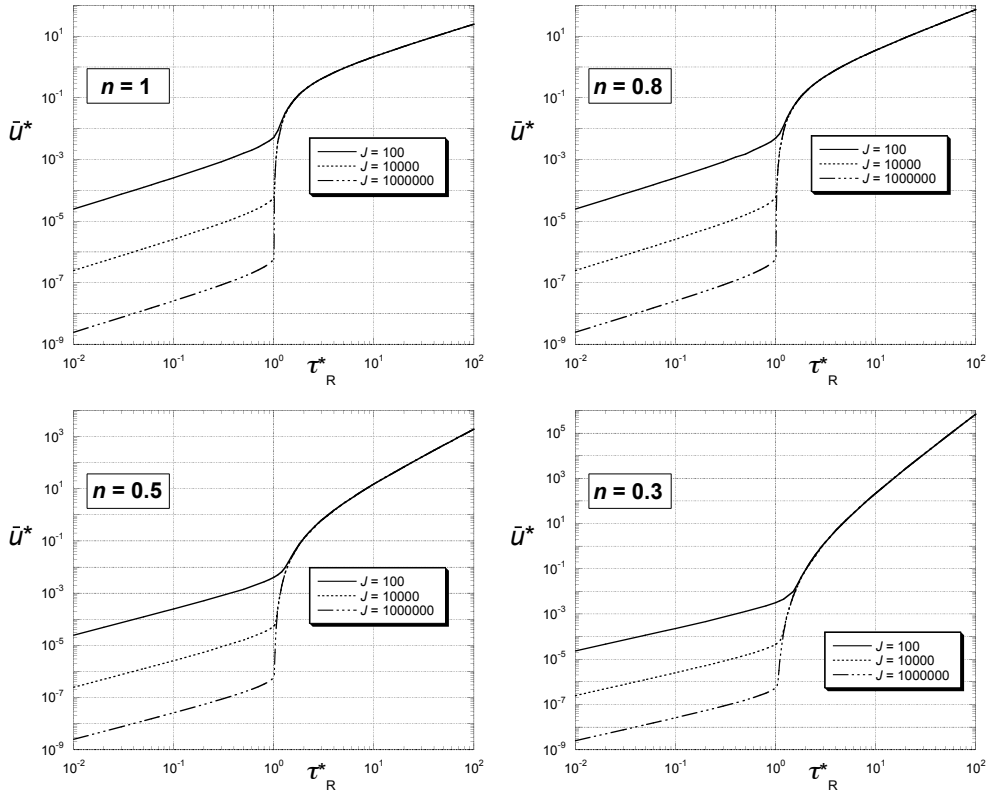

Figure IV.6: Dimensionless average velocity as a function of the dimensionless wall shear stress.

The average axial velocity $\bar{u}^*$ is obtained from

$$\bar{u}^* = 2\int_0^1 u^* r^* dr^* \tag{15}$$

Fig. IV.6 shows the dimensionless average velocity as a function of the dimensionless wall shear stress for different values of the jump number. A steep increase in average velocity is observed just beyond $\tau_R^* = 1$. As τ_R^* is further increased, the curves for different J values merge, at $\bar{u}^* \simeq 1/J$, into the $J \to \infty$ envelope curve.

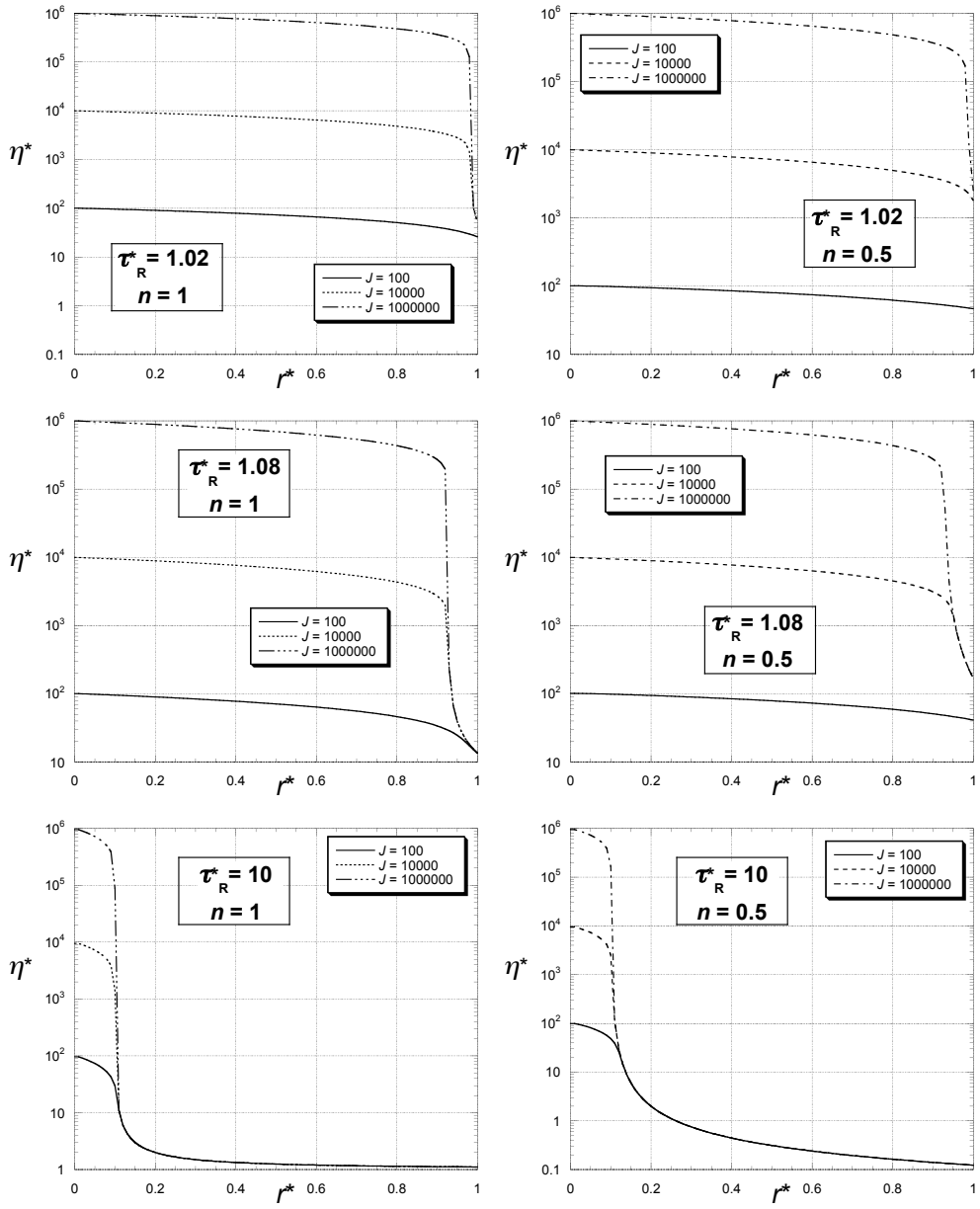

Figure IV.7: Dimensionless viscosity profiles.

These results demonstrate the existence of three distinct flow regimes, depending on the range of τ_R^*:

- when $\tau_R^* \leq 1$, a *Newtonian flow regime* is observed, with a dimensionless average velocity $\bar{u}^* < 1/J$;
- when $1 < \tau_R^* < f(n)$, a *lubricated-plug flow regime* is observed. The function $f(n)$ is the value of τ_R^* corresponding to $\bar{u}^* = 1$. From Fig. IV.6 it is seen that $2.9 \lesssim f(n) \lesssim 5$ for $0.3 < n < 1$. In this range the average velocity increases from $1/J$ up to 1, very steeply in the vicinity of $\tau_R^* = 1$ and progressively less steeply as τ_R^* increases towards $f(n)$;

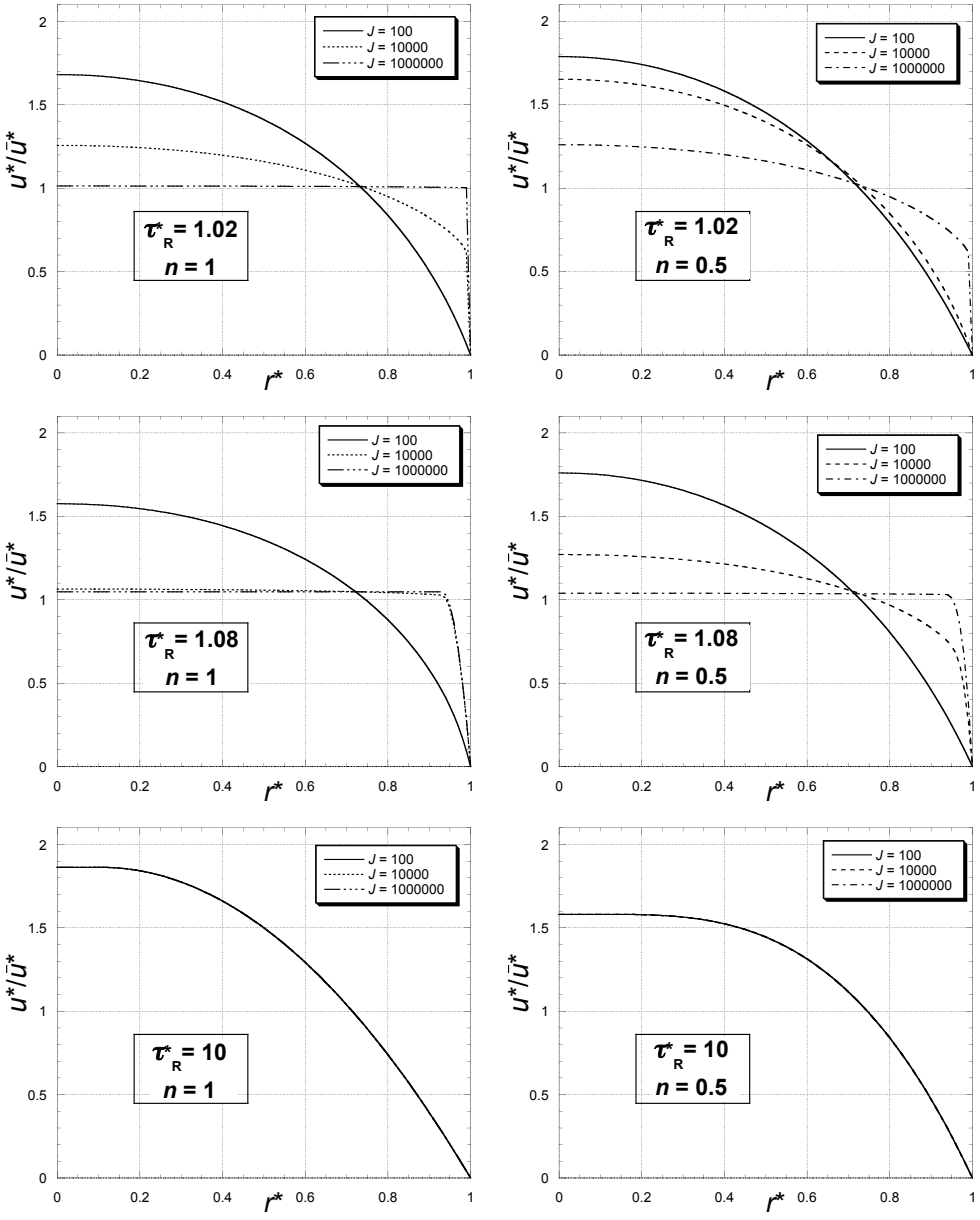

Figure IV.8: Dimensionless velocity profiles.

– at the other end when $\tau_R^* > f(n)$, a *power-law flow regime* is observed, i.e. the flow rate is no longer affected by the viscoplastic nature of the material.

The viscosity profiles shown in Fig. IV.7 illustrate the important viscosity changes that occur for high jump numbers in the vicinity of the radial position where the shear stress equals the yield stress. When this radial position is close to the tube wall, a thin layer of low-viscosity, lubricating liquid is observed, causing the steep flow rate increases observed in the lubricated-plug flow regime.

Fig. IV.8 illustrates the shape of the axial velocity profile for different

values of J, n, and τ_R^*. As illustrated in the graphs pertaining to τ_R^* values closer to unity, the jump number dictates the shape of the velocity profile. For example, it can be observed that the velocity profile for the case $n = 0.5$, $J = 10^6$ undergoes a significant change as τ_R^* is further increased from 1.02 (Fig. IV.8, top right graph) to 1.08 (Fig. IV.8, middle right graph). This change is explained as follows. For this case, when $\tau_R^* = 1.02$, the thickness of the low-viscosity layer, say δ, is so small that the velocity jump across it, $\dot{\gamma}_1\delta$, is still negligible. As τ_R^* is further increased to 1.08, δ increases enough to render $\dot{\gamma}_1\delta$ large, modifying the velocity profile and causing the flow rate jump illustrated in Fig. IV.6. However, it is seen from the last two graphs ($\tau_R^* = 10$) that, for wall shear stress values much larger than the yield stress (power-law flow regime), the jump number has essentially no effect on the profile shape, because most of the material in the flow domain is yielded.

For a given value of τ_R^* within the lubricated-plug flow regime, the thickness δ of the low-viscosity layer is a function of the jump number, as inferred from Figs. IV.7 and IV.8. As it will be discussed shortly, the fractional mass coverage m and the low-viscosity layer thickness δ are closely related.

(b) Fractional mass coverage results

The foregoing discussion for the fully developed-flow that occurs ahead of the bubble provides the basis for understanding the observations made during the displacement experiments, to be presented in what follows.

In a typical set of experiments with a given Carbopol dispersion, at low flow rates it is possible to observe perfect displacements and low-curvature air-liquid interfaces, whereas imperfect displacements and higher-curvature bubble fronts were observed for higher flow rates.

Figure IV.9 shows the air-liquid interfaces for the four viscoplastic materials investigated, corresponding to $Ca_p = 0.20$, 0.45, 0.83, and 2.0. For each of these materials, the picture of the interface is shown for four different flow rates, i.e. the picture on the left pertains to a very low value of $\bar{u}^*$, and the subsequent pictures towards the right pertain to progressively larger values of $\bar{u}^*$. Table IV.1 gives the values of Ca_p, $\bar{u}^*$, τ_R^*, and m corresponding to each of the pictures shown in Fig. IV.9.

It is seen in these pictures that, for each material, the interface curvature increases as $\bar{u}^*$ is increased. Moreover, the thickness of the layer of viscoplastic material left on the tube wall increases as $\bar{u}^*$ is increased. Actually, in the left-hand side pictures (very low-$\bar{u}^*$ cases) of Fig. IV.9, no material seems to be left behind, i.e. the displacement seems to be perfect. For the higher-Ca_p cases, the interface remains undeformed because most of the material is un-

yielded. It is worth emphasizing that a perfect displacement is not observed for Newtonian or viscoelastic materials (e.g. [68, 75, 76, 87]).

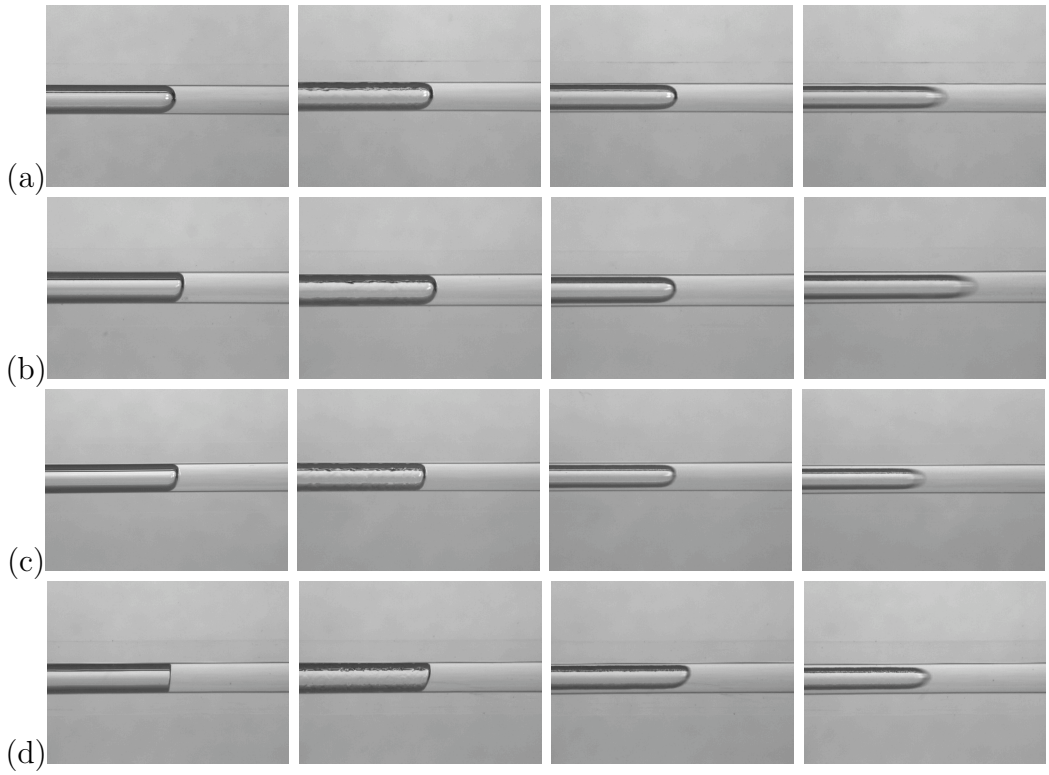

Figure IV.9: Interface shapes. (a) Carbopol 0.09%; (b) Carbopol 0.11%; (c) Carbopol 0.15%; (d) Carbopol 0.17%. The bubble speed increases from left to right; see Table IV.1 for the corresponding Ca_p, $\bar{u}^*$, τ_R^*, and m values.

As the material yields (at higher $\bar{u}^*$'s), the air penetrates into the material and the interface curvature increases, and a layer of material is left behind on the wall. This layer remains static and unyielded. The pictures on the second column in Fig. IV.9 (low-$\bar{u}^*$ cases) illustrate the early stages of deposition, when only small lumps of unyielded material are left on the wall. This observation may be related to instabilities of the type reported by Gabard and Hulin [81]. As the average velocity is further increased (medium and fast flow cases), the amount of material left behind on the wall increases, and a smooth layer of nearly-uniform[1] thickness is observed. The approximate maximum Reynolds number values achieved were 0.8 for air and 0.3 for the Carbopol dispersions.

[1]A mild buoyancy effect was present in the experiments, displacing the bubble upwards and somewhat distorting the interface.

Table IV.1: Plastic capillary number, flow rate, and wall shear stress values of the flows shown in Fig. IV.9.

	Conc. (%)	Ca_p	$\bar{u}^*$	τ_R^*	m
very slow flow	0.09	0.20	0.058	1.8	0.013
	0.11	0.45	0.022	1.6	0.037
	0.15	0.83	0.036	1.7	0.019
	0.17	2.00	0.17	2.2	0.037
slow flow	0.09	0.20	0.21	2.2	0.024
	0.11	0.45	0.10	2.0	0.0055
	0.15	0.83	0.65	2.8	0.0056
	0.17	2.00	0.60	2.7	0.053
medium flow	0.09	0.20	2.3	4.2	0.12
	0.11	0.45	1.0	3.2	0.11
	0.15	0.83	4.2	4.3	0.15
	0.17	2.00	1.2	3.2	0.096
fast flow	0.09	0.20	14	7.8	0.30
	0.11	0.45	7.2	5.7	0.31
	0.15	0.83	8.6	5.3	0.26
	0.17	2.00	5.2	4.6	0.28

The fractional mass coverage m is given in Fig. IV.10 as a function of the average velocity, $\bar{u}^*$, as obtained in the displacement experiments described in Sec. IV.3(a). Average velocities within the Newtonian flow regime ($\tau_R^* < 1$) are too low to be perceived with our experimental procedure. Therefore, the lowest $\bar{u}^*$ values investigated corresponded to τ_R^* values larger than unity, i.e. in the lubricated-plug flow regime characterized by $1/J \leq \bar{u}^* \leq 1$, and in the power-law flow regime when $\bar{u}^* > 1$ (see Fig. IV.6 and the discussion in Sec. IV.4(a)).

For the materials investigated, there is a threshold or critical average velocity, $\bar{u}^*_{crit}$, below which the displacement is perfect ($m = 0$) within the measurement capability of the experimental procedure. The data illustrate that $0.1 \lesssim \bar{u}^*_{crit} \lesssim 2$ for the four Carbopol dispersions investigated, i.e. it is in the close vicinity of the upper limit of the lubricated-plug flow regime. Below this critical average velocity, the viscoplastic material seems to move inside the capillary as a rigid body. The fully-developed flow results discussed above suggest that this seemingly rigid-body motion is actually a flow in the lubricated-plug flow regime such that its low-viscosity layer is too thin to be observable. Therefore, the amount of yielded material available to be left deposited on the wall is negligible. Above the critical average velocity $\bar{u}^*_{crit}$, the low-viscosity layer is thick enough to provide a measurable mass of material that is left behind on the tube wall. Hence, m departs from zero and starts to

increase monotonically with $\bar{u}^*$.

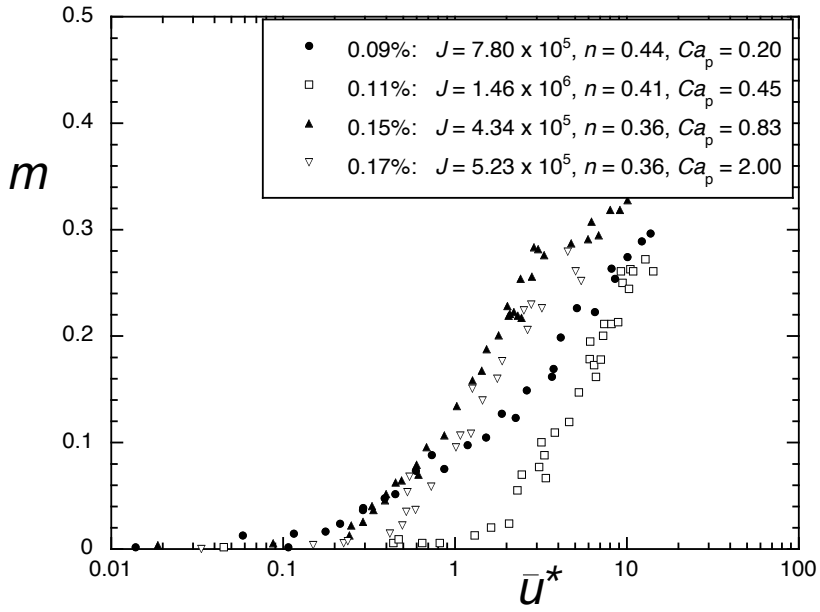

Figure IV.10: The fractional mass coverage as a function of the average velocity.

The data in Fig. IV.10 suggests that the plastic capillary number Ca_p governs the slope $dm/d\bar{u}^*$ of the $m \times \bar{u}^*$ curves at $m = 0$. More specifically, $dm/d\bar{u}^*$ at $m = 0$ increases as Ca_p is increased. Indeed, for Newtonian and viscoelastic materials ($Ca_p = 0$), the results available in the literature show that this slope is very small in the low-flow rate (or capillary number) range, where m is very small. In the power-law flow regime, m is expected not to depend on the plastic capillary number, because much of the material is yielded, and hence the relative importance of the yield stress at the interface becomes small.

For intermediate values of m ($0.1 \lesssim m \lesssim 0.25$), the slope of the curves becomes roughly the same. In this range, where the average velocity values are $\bar{u}^* \lesssim 6$, the corresponding fully-developed wall shear stress values are $\tau_R^* \lesssim 6$. Fig. 6 shows that the power-law exponent n does not affect significantly the (dimensionless) viscosity function in this range of shear stress, and hence it should not affect the m curves either. Therefore, m should depend on J only. Indeed, in this range the curves are positioned with respect to each other according to their jump number values, J increasing from left to right. Thus, for a given flow rate $\bar{u}^*$, m decreases as J is increased. This behavior is consistent with the dependence of the velocity profiles on the jump number, illustrated in

Fig. IV.8. This figure shows that the thickness of the layer of yielded material decreases as the jump number is increased.

For larger values of $\bar{u}^*$ (and hence larger values of m), the slopes of the m curves decrease, and this trend is more pronounced for the curves pertaining to lower jump number values. In the range of $\bar{u}^*$ well within the power-law flow regime, the shear stresses are within the range where the viscosity depends strongly on the power-law exponent n and does not depend on the jump number J (Fig. 6). Thus, in the transition range where the jump number influence diminishes while the influence of the power-law exponent increases, the m curves for the four Carbopol dispersions tend to approach each other as $\bar{u}^*$ is increased. Indeed, from the behavior already established for Newtonian liquids, is seems reasonable to expect that, at sufficiently large values of $\bar{u}^*$ such that the flow is well within the power-law regime, the four curves reach asymptotic values that depend on the power-law exponent only. However, large enough flow rates could not be achieved with the experimental setup employed, and hence the just described expected trend remains to be verified.

Finally for this section, it is illustrative to discuss what it is expected to occur in the range $\tau_R^* < 1$, which was not explored in the experiments due to the extremely low velocities. In this range the Carbopol dispersions behave as Newtonian liquids with viscosity η_o. Hence, Taylor's Newtonian $m \times Ca$ curve [71] should be applicable for $Ca = \eta_o U/\sigma \lesssim Ca_p/(1-m)$ (or $\bar{u}^* \lesssim 1/J$), i.e. when $\tau_R^* < 1$.

IV.5 Final Remarks

An investigation about the displacement of viscoplastic materials in capillary tubes by gas injection was reported in this chapter. The research encompassed experiments with Carbopol aqueous dispersions and an analysis of the fully-developed flow of the viscoplastic materials alone [26], to aid in the understanding of the experimental flow-displacement results.

The measured viscosity data were fitted to the viscosity function proposed by de Souza Mendes and Dutra [24]. This equation was made dimensionless with the aid of its own parameters only, giving rise to the jump number, a novel rheological property of viscoplastic materials.

The results obtained showed that, below a certain critical flow rate, the viscoplastic material is perfectly displaced by the pushing gas. Just above this critical flow rate, which depends on the jump number, small lumps of unyielded material begin to deposit on the tube wall. As the flow rate is further increased, a smooth material layer of uniform thickness begins to form. The thickness

of the layer is observed to increase with the dimensionless flow rate and to decrease as the jump number is increased.

IV.6 Note

In this chapter it was realized an analysis of the displacements of viscoplastic materials in capillary tubes. Sec. IV.1 is a bibliography review about the subject performed by prof. de Souza Mendes. In Sec. IV.2 the governing equations found in the bibliography review are shown. In Sec. IV.3 the experiments realized by José Roberto Siffert in partnership with myself and Eduardo Dutra are described. It is important to point out that when I started to work in this research the paper had already been submitted, so that my name does not appear in the publication. Although, after I started to work in this research all experimental results were redone. I spent a lot of time developing the techniques used to capture the images taken and shown in this chapter. I also worked hard in the techniques of Carbopol dispersions preparation. I characterized all of the dispersions used, and collaborated with the fraction mass measurements. Thus, this chapter is in my thesis. The results of this research are shown and discussed in Sec. IV.4, and some final remarks can be found in Sec. IV.5. This research in which I collaborated was led by prof. de Souza Mendes.